




Discrete and Continuous Ejection Models of the Radio Source Associated with GW170817

Brian Punsly^{1,2,3} 

¹ 1415 Granvia Altamira, Palos Verdes Estates CA 90274, USA; brian.punsly@cox.net

² ICRANet, Piazza della Repubblica 10 Pescara 65100, Italy

³ ICRAN, Physics Department, University La Sapienza, Roma, Italy

Received 2018 December 6; revised 2019 January 20; accepted 2019 January 23; published 2019 February 4

Abstract

The gravity wave source, GW170817, and associated gamma-ray burst (GRB), GRB 170817A, produced radio emission that was detected in multiple epochs of Very Long Baseline Interferometry (VLBI) and with broadband radio photometry. Three unique pieces of observational evidence were determined: a discrete radio-emitting region that moves with an apparent velocity of $\approx 4c$, a discrete region that includes all of the radio flux, and a likely synchrotron self absorption (SSA) spectral turnover on day ~ 110 and day ~ 160 after ejection. This unprecedented wealth of data for a GRB provides a unique opportunity to understand the radio-emitting plasma that was ejected by the putative merger event. The velocity can constrain the kinematics, and the SSA turnover has been used to constrain the size to one that is much smaller than can be done with an unresolved VLBI image, allowing one to estimate the associated plasmoid size directly from the data and improve estimates of the energetics. Models of the radio emission for both a turbulent, protonic, discrete ballistic ejection and a high dissipation region within an otherwise invisible Poynting flux dominated positron–electron jet are considered. On days ~ 110 and ~ 160 post-merger, for the range of models presented, the jet power is 2×10^{39} – 8×10^{40} erg s^{−1} and the ballistic plasmoid kinetic energy is 3×10^{45} – 1.5×10^{47} erg. Even though only valid after day 110, this independent analysis augments traditional GRB light curve studies, providing additional constraints on the merger event.

Key words: accretion, accretion disks – black hole physics – X-rays: binaries

1. Introduction

The gravitational wave (GW) detection, GW170817, by the Laser Interferometer Gravitational-Wave Observatory (LIGO) and Virgo on 2017 August 17, was accompanied by a short gamma-ray burst (GRB), GRB 170817A, detection by *FERMI* (Abbott et al. 2017a, 2017b; Goldstein et al. 2017). The GRB is believed to be associated with a merger event with a stellar-mass compact remnant (Abbott et al. 2017b; Rueda et al. 2018). This is the first association of an electromagnetic signal with a GW and has received extensive monitoring over the last year. Monitoring has revealed a wealth of information that has generally not been available for other GRBs. There have been many attempts to analyze this event by methods traditionally used for other GRBs with less observational information, namely a light curve power-law analysis (Hallinan et al. 2017; Dobie et al. 2018; Mooley et al. 2018a, 2018c; Troja et al. 2018a, 2018b). The results suggested a more complicated time evolution than was typical for GRBs in order to explain the rising X-ray emission over the first three months. The detection of a moving radio component with an apparent velocity, $v_{\text{app}} \approx 4c$, is direct observational evidence that restricts the kinematics (Mooley et al. 2018a). The discrete component that was detected with Very Long Baseline Interferometry (VLBI; $\sim 10,000$ km baselines) at 4.5 GHz on day 75–day 230 after the merger had the same flux density as that found on ~ 25 km baselines with the Jansky Very Large Array (JVLA; Ghirlanda et al. 2018; Mooley et al. 2018a). This indicates that all of the detected radio flux from this event is contained in the single moving unresolved component. This appears to be directly analogous to the most powerful ejections from stellar-mass compact objects in the Galaxy, the superluminal discrete ejections, or major flares (Mirabel & Rodriguez 1994;

Fender et al. 1999). Thus motivated, a treatment of the radio-emitting ejection associated with GW170817 in direct analogy to previous analysis of stellar-mass black holes with superluminal discrete ejections in the Galaxy is presented.

In the Galaxy, discrete superluminal ejections have been interpreted as either a moving, strong dissipation region in a continuous relativistic jet or a discrete ballistic ejection (Fender et al. 2004; Punsly 2012). Similarly, the model chosen for GW170817 is one in which all of the emission is from a single moving unresolved component with no detected emission from a stationary core or a smooth background jet. Because the emission is unresolved, no structure is ascertained and a simple spherical homogeneous volume is assumed. The region can be considered a discrete ballistic plasmoid that was ejected along a preferred axis (such as a total angular momentum axis) as a byproduct of the merger event. Alternatively, if one assumes a continuous jet, then the spherical dissipation region might be the advancing head of the jet, akin to a radio lobe or hot spot in an extragalactic radio source. The unresolved VLBI image restricts the size to $< 10^{17}$ cm, (Ghirlanda et al. 2018). However, for the spherical volume, if the spectrum appears as a power law with a low frequency (synchrotron self-absorbed (SAA)) turnover, one can obtain an estimate of the spatial dimension that can be much less than the unresolved image (Reynolds et al. 2009). This dimensional estimate can be used to improve estimates of the energetics of the ejection if the bulk-flow Doppler factor of the plasmoid, δ , is estimated from the observed kinematics (Punsly 2012; Lightman et al. 1975),

$$\delta = \frac{\gamma^{-1}}{1 - \beta \cos \theta}, \quad \gamma^{-1} = 1 - \beta^2, \quad (1)$$

where β is the normalized three-velocity of bulk motion and θ is the angle of the motion to the line of sight (LOS) to the

observer. These methods are presented in Section 2. They were first developed to describe discrete ejections from the quasar, Mrk 231, and was later applied to the major ejections from the Galactic black hole (GBH) GRS 1915 + 105 (Reynolds et al. 2009; Punsly 2012).

In Section 3, the model is constrained by the radio spectra on days ~ 110 and ~ 160 . These constraints and the apparent velocity of $4c$ are used to explore the physical solution space of the models in Section 4. The results are analyzed in Section 5.

2. SSA Homogeneous Plasmoids

As the ejection is unresolved, the simple homogeneous spherical volume model of van der Laan (1966) is chosen. The strategy will be to evaluate in the rest frame then transform the results to the observer's frame for comparison with observation. The underlying power law for the flux density is defined by $S_\nu(\nu = \nu_o) = S\nu_o^{-\alpha}$, where S is a constant. Observed quantities will be designated with a subscript, "o," in the following expressions. The SSA attenuation coefficient in the plasma rest frame (noting that the emitted frequency is designated by ν) is given by (Ginzburg & Syrovatskii 1969),

$$\mu(\nu) = \overline{g(n)} \frac{e^3}{2\pi m_e} N_\Gamma (m_e c^2)^{2\alpha} \left(\frac{3e}{2\pi m_e^3 c^5} \right)^{\frac{1+2\alpha}{2}} \times (B)^{(1.5+\alpha)} (\nu)^{-(2.5+\alpha)}, \quad (2)$$

$$\overline{g(n)} = \frac{\sqrt{3\pi} \Gamma[(3n+22)/12] \Gamma[(3n+2)/12] \Gamma[(n+6)/4]}{8 \Gamma[(n+8)/4]}, \quad (3)$$

$$N = \int_{\Gamma_{\min}}^{\Gamma_{\max}} N_\Gamma \Gamma^{-n} d\Gamma, \quad n = 2\alpha + 1, \quad (4)$$

where Γ is the ratio of lepton energy to rest mass energy, $m_e c^2$, and $\overline{\Gamma}$ is the gamma function. B is the magnitude of the total magnetic field. The power-law spectral index for the flux density is $\alpha = (n-1)/2$. The low energy cutoff, $E_{\min} = \Gamma_{\min} m_e c^2$, is not constrained by the data. The SSA opacity in the observer's frame, $\mu(\nu_o)$, is obtained by direct substitution of $\nu = \nu_o/\delta$ into Equation (2). The homogeneous approximation yields a simplified solution to the radiative transfer equation (Ginzburg & Syrovatskii 1965; van der Laan 1966)

$$S_{\nu_o} = \frac{S_o \nu_o^{-\alpha}}{\tau(\nu_o)} \times (1 - e^{-\tau(\nu_o)}), \quad (5)$$

$$\tau(\nu_o) \equiv \mu(\nu_o) L, \quad \tau(\nu_o) = \overline{\tau} \nu_o^{-(2.5+\alpha)},$$

where $\tau(\nu)$ is the SSA opacity, L is the path length in the rest frame of the plasma, S_o is a normalization factor, and $\overline{\tau}$ is a constant. There are three unknowns in Equation (5), $\overline{\tau}$, α , and S_o . These are the three constraints on the following theoretical model that are estimated from the observational data.

The theoretical spectrum is parameterized by Equations (2)–(5) and the synchrotron emissivity that is given in Tucker (1975) as

$$j_\nu = 1.7 \times 10^{-21} [4\pi N_\Gamma] a(n) B^{(1+\alpha)} \left(\frac{4 \times 10^6}{\nu} \right)^\alpha, \quad (6)$$

$$a(n) = \frac{(2^{\frac{n-1}{2}} \sqrt{3}) \overline{\Gamma} \left(\frac{3n-1}{12} \right) \overline{\Gamma} \left(\frac{3n+19}{12} \right) \overline{\Gamma} \left(\frac{n+5}{4} \right)}{8 \sqrt{\pi} (n+1) \overline{\Gamma} \left(\frac{n+7}{4} \right)}. \quad (7)$$

One can transform this to the observed flux density, $S(\nu_o)$, in the optically thin region of the spectrum using the relativistic transformation relations from Lind & Blandford (1985),

$$S(\nu_o) = \frac{\delta^{(3+\alpha)}}{4\pi D_L^2} \int j'_\nu dV', \quad (8)$$

where D_L is the luminosity distance and in this expression, the primed frame is the rest frame of the plasma.

3. Fitting the Data

The epochs of days 107–115 (epoch 1) and days 152–163 (epoch 2), near the peak of radio flux light curves, are densely sampled in frequency from 1.25 to 17 GHz. Dense frequency sampling is essential for an accurate estimate of α because the flux density is very low, ~ 20 – $100 \mu\text{Jy}$. "Small" unanticipated systematic errors can drastically skew an individual measurement. This is clear by the outlier points in Figure 1. The other essential feature is the need for low-frequency Giant Metre-wave Radio Telescope (GMRT) measurements in order to determine the magnitude of the SSA. The ejection is clearly resolved from the host galaxy nuclear radio source by GMRT at 1.25 GHz, but only marginally resolved at 675 MHz (Resmi et al. 2018). The analysis of this Letter relies primarily on the modeling of epochs 1 and 2 that are not contemporaneous with the difficult 675 MHz Gaussian model fits.

Mathematically, the theoretical determination of S_ν depends on seven parameters in Equations (2)–(8), N_Γ , B , R (the radius of the sphere), α , δ , E_{\min} , and E_{\max} , yet there are only three constraints from the observation $\overline{\tau}$, α , and S_o , it is an underdetermined system of equations. Most of the particles are at low energy, so the solutions are insensitive to E_{\max} . In order to study the solution space, δ and E_{\min} are pre-set to a 2D array of trial values. For each trial value one has four unknowns, N_Γ , B , R , and α , and three constraints for each model. Thus, there is an infinite 1D set of solutions for each pre-assigned δ and E_{\min} that results in the same spectral output. First, a least squares power-law fit, with uncertainty in both variables, is made between ~ 3 and 17 GHz (Reed 1989). This fixes S_o and α in Equation (5). An arbitrary B is chosen. N_Γ and R are then iteratively varied to produce this fitted S_o and a value of $\overline{\tau}$ that minimizes the least squares residuals relative to the GMRT data in Figure 1. Another value of B is chosen and the process is repeated until the solution space is spanned for the pre-assigned δ and E_{\min} . For epoch 1 (epoch 2), $\alpha = 0.49 \pm 0.05$ ($\alpha = 0.54 \pm 0.06$).

The bottom frames of Figure 1 indicate that the power law derived from the higher-frequency data greatly exceeds the 675 MHz flux density, justifying the SSA model over the power-law model. Epoch 1A (bottom right), day 102.5–112, is an attempt at a quasi-simultaneous fit that includes the 675 MHz data. This fit might be less robust due to the difficult 675 MHz data reduction.

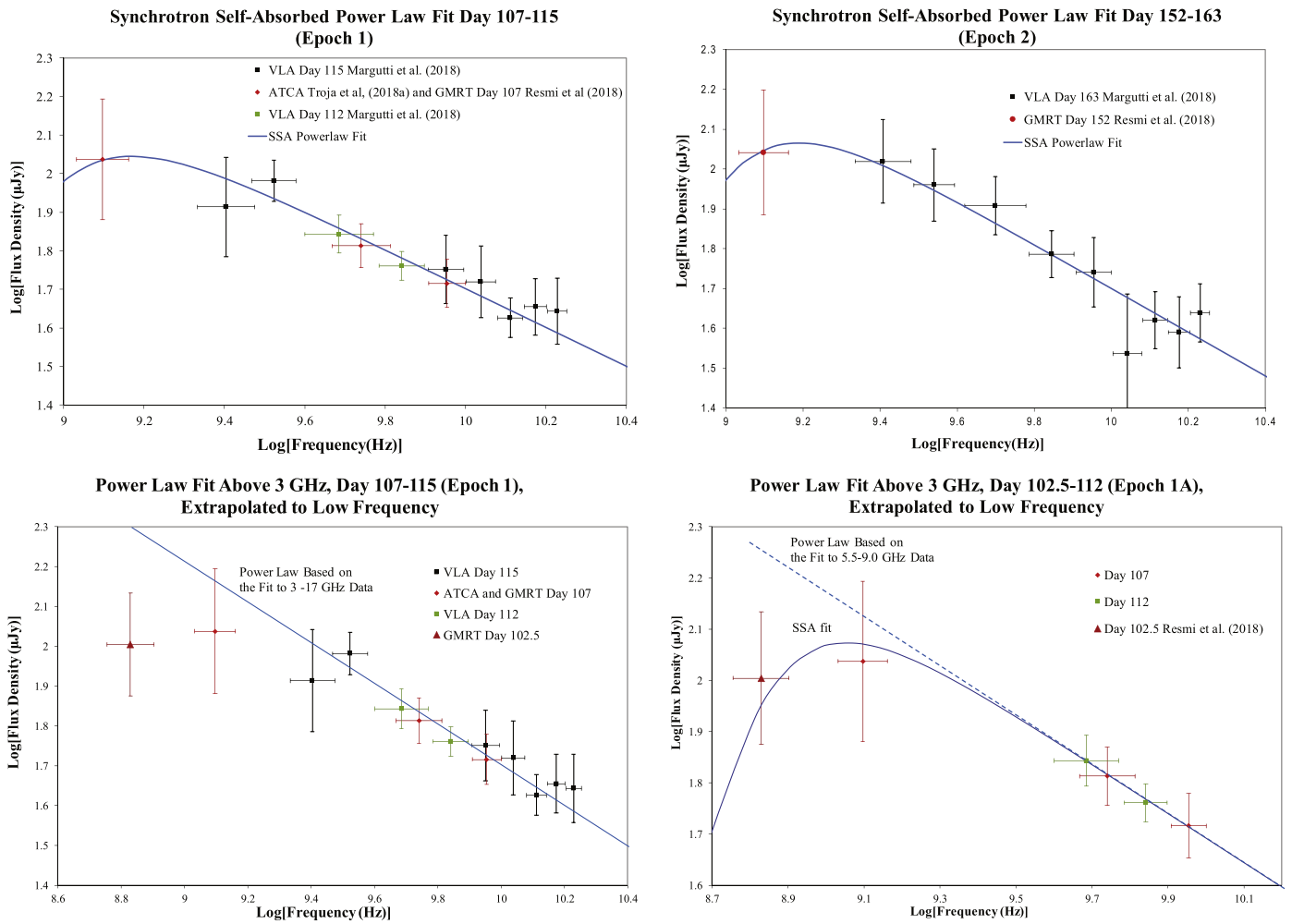


Figure 1. The top-left (top-right) frame is the radio data from epoch 1 (epoch 2). The SSA power-law fits of Equation (5) are the continuous curves (see Sections 2 and 3). The bottom frames extrapolate the power-law fit above 3 GHz to lower frequency revealing an excess at 675 MHz. The data in this figure is from Margutti et al. (2018), Troja et al (2018a), and Resmi et al (2018).

Doppler Factor for an Apparent Velocity of $4c$ as a Function of the Line of Sight

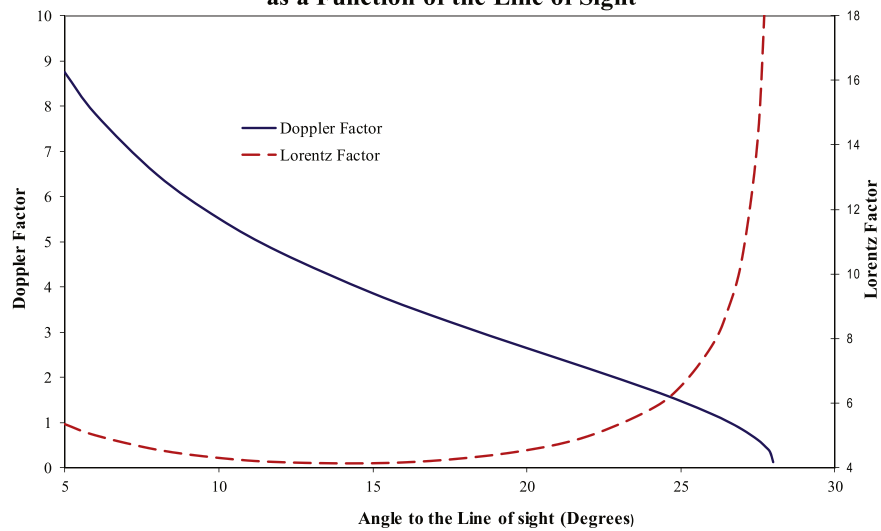


Figure 2. Detection of superluminal motion, $4c$, restricts δ , LOS, and γ .

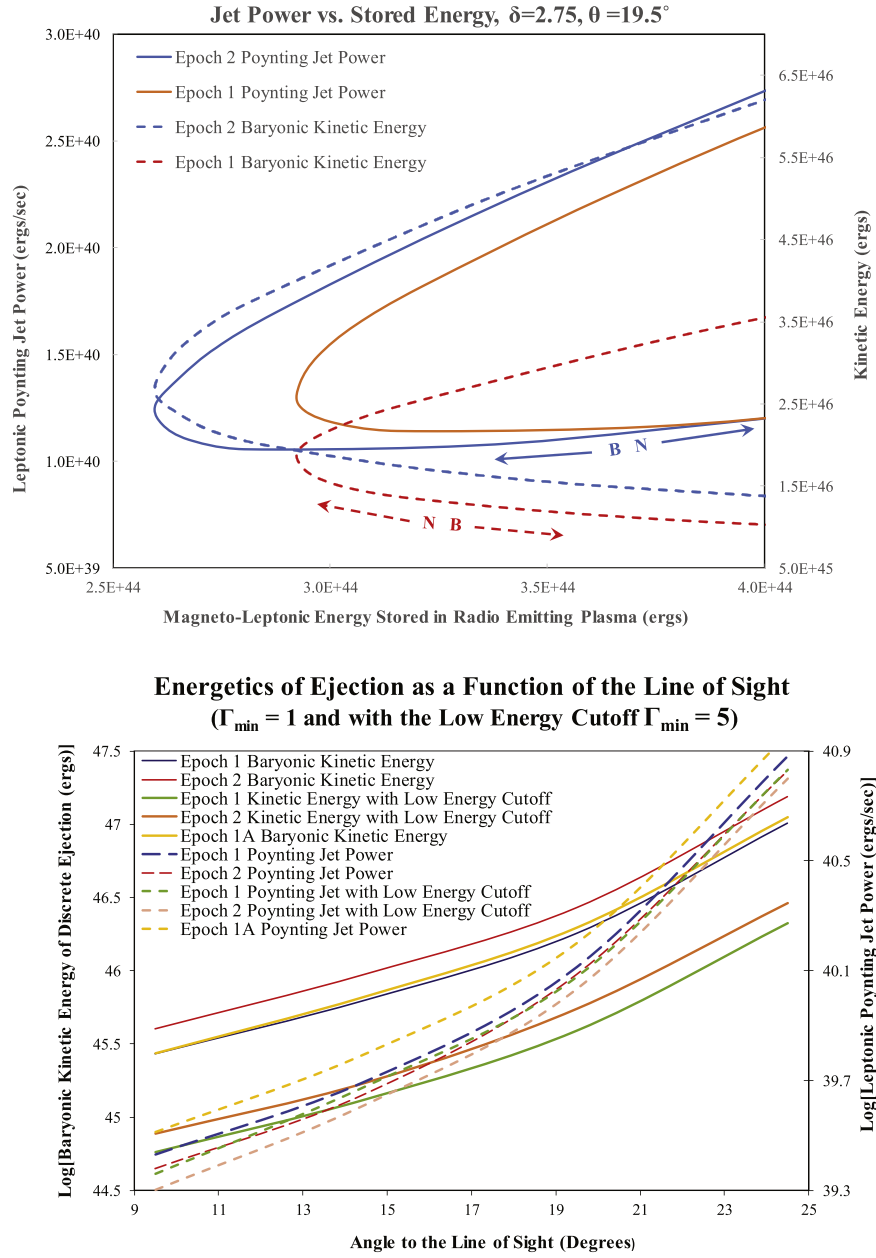


Figure 3. The top panel shows the dependence of bulk kinetic energy of a discrete ejection and the jet power on E_m for one LOS. The behavior is similar for other LOS. The bottom panel shows how they depend on the LOS, using the restrictions from Figure 2 and assuming the minimum E_m .

4. Specific Spherical Models

The apparent velocity constrains the kinematics of the plasmoid (Rees 1966):

$$v_{\text{app}}/c = \beta_{\text{app}} = \beta \sin \theta / (1 - \beta \cos \theta) \approx 4. \quad (9)$$

Equations (1) and (9) are combined in Figure 2 in order to restrict δ . The superluminal motion indicates a LOS $< 28^\circ$. The top and middle panels of Figure 1 shows the fits to the data for 1D sets of models that exist for each chosen pair of values of Γ_{\min} and δ . Using Figure 2 to restrict δ , the physical parameters associated with a continuous range of models are displayed graphically in Figures 3 and 4 for $\Gamma_{\min} = 1$ and $\Gamma_{\min} = 5$. For the ballistic ejection the magnetic field is turbulent, and for a jet it is mainly organized toroidal magnetic field, B'_ϕ , in the rest frame of the plasma. The latter is a

consequence of the perfect magnetohydrodynamic (MHD) assumption and approximate angular momentum conservation in the jet (Blandford & Königl 1979). The total angular momentum flux along the jet axis in the observer's coordinate system is (Punsly 2008)

$$L \approx k \mu r_\perp \gamma v^\phi + \frac{c}{4\pi} B^\phi r_\perp^2, \quad k \equiv \frac{\mathcal{N} \gamma v^P}{B^P}, \quad (10)$$

where k is the perfect MHD conserved mass flux per unit poloidal magnetic flux, B^P and v^P are the poloidal magnetic field and velocity, \mathcal{N} is the number density in the plasma rest frame, μ is the specific enthalpy, and r_\perp is the cylindrical radius. As the jet propagates, it expands and r_\perp is much larger than at the jet base. By Equation (10), if L is approximately constant and the jet is Poynting flux dominated, or the

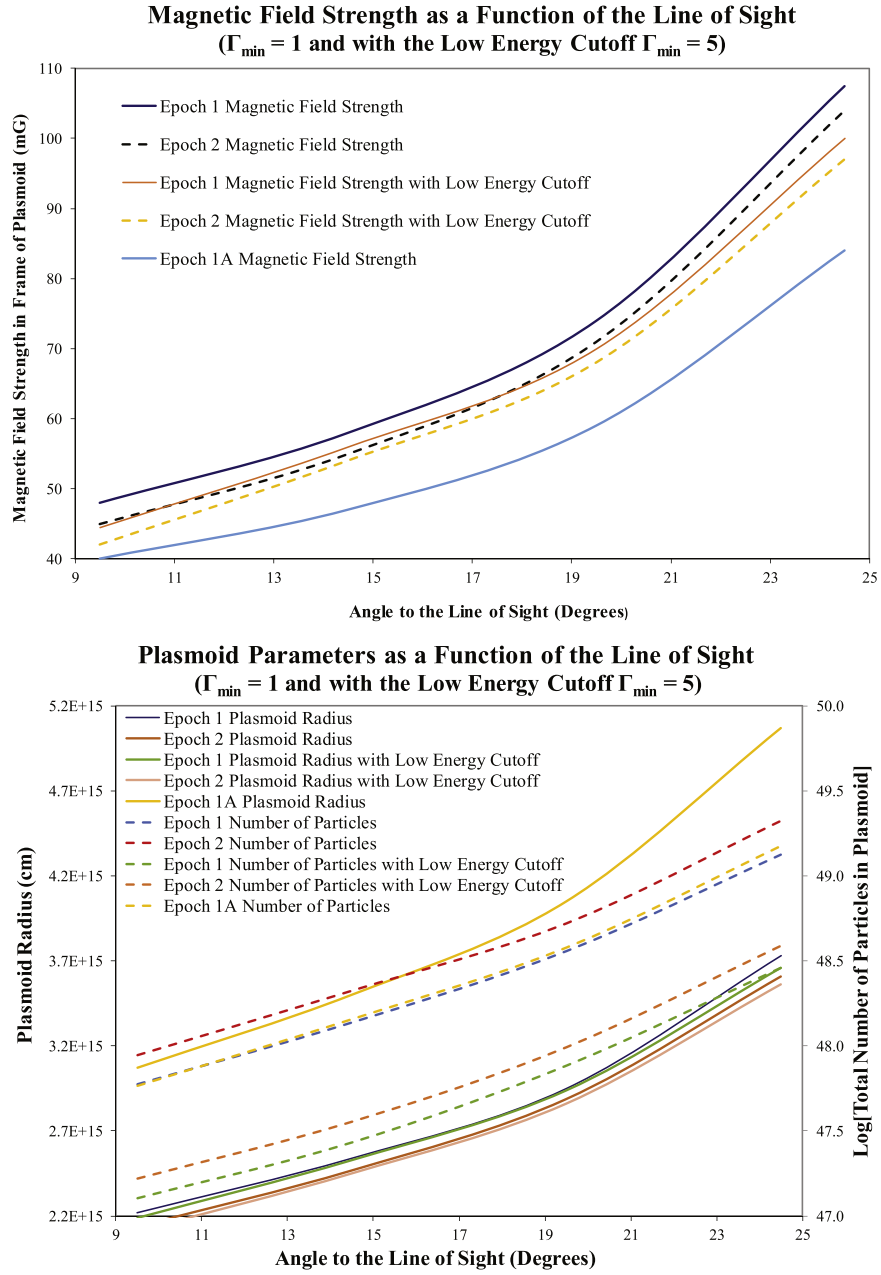


Figure 4. The top (bottom) panel shows how B (R and the total number of particles in the plasmoid) in the spherical models depends on the LOS, assuming the minimum E_{lm} .

mechanical angular momentum and the electromagnetic angular momentum are comparable (which can occur at the head of the jet), with large r_{\perp} ,

$$v^{\phi} < \frac{L}{k\mu r_{\perp} \gamma} \quad B^{\phi} \sim r_{\perp}^{-\eta}, \quad \eta \approx 1. \quad (11)$$

By poloidal magnetic flux conservation $B^P \sim r_{\perp}^{-2}$, so $B^{\phi} \gg B^P$ at large r_{\perp} . To estimate the poloidal Poynting flux, S^P , in the plasmoid, first transform fields to the observer's frame

$$B^{\phi} = \gamma B'_{\phi} \quad E^{\perp} = \frac{v^P}{c} \gamma B'_{\phi} - \frac{v^{\phi}}{c} \gamma B^P \approx \frac{v^P}{c} \gamma B'_{\phi}, \quad (12)$$

where E^{\perp} is the poloidal electric field orthogonal to the magnetic field direction. The poloidal Poynting flux in the

observer's frame, S^P , along the jet direction is (Punsly 2008):

$$S^P = \frac{c}{4\pi} E^{\perp} B^{\phi} \approx \frac{c}{4\pi} \gamma^2 \beta [B'_{\phi}]^2, \quad B'_{\phi} \approx B. \quad (13)$$

The energy content is separated into two pieces. The first is the kinetic energy of the protons, $E(\text{proton})$. The other piece is named the lepto-magnetic energy, $E(\text{lm})$, and is composed of the volume integral of the leptonic internal energy density, U_e , and the magnetic field energy density, U_B . It is straightforward to compute the lepto-magnetic energy in a spherical volume,

$$E(\text{lm}) = \int (U_B + U_e) dV = \frac{4}{3} \pi R^3 \left[\frac{B^2}{8\pi} + \int_{\Gamma_{\min}}^{\Gamma_{\max}} (m_e c^2) (N_{\Gamma} E^{-n+1}) dE \right]. \quad (14)$$

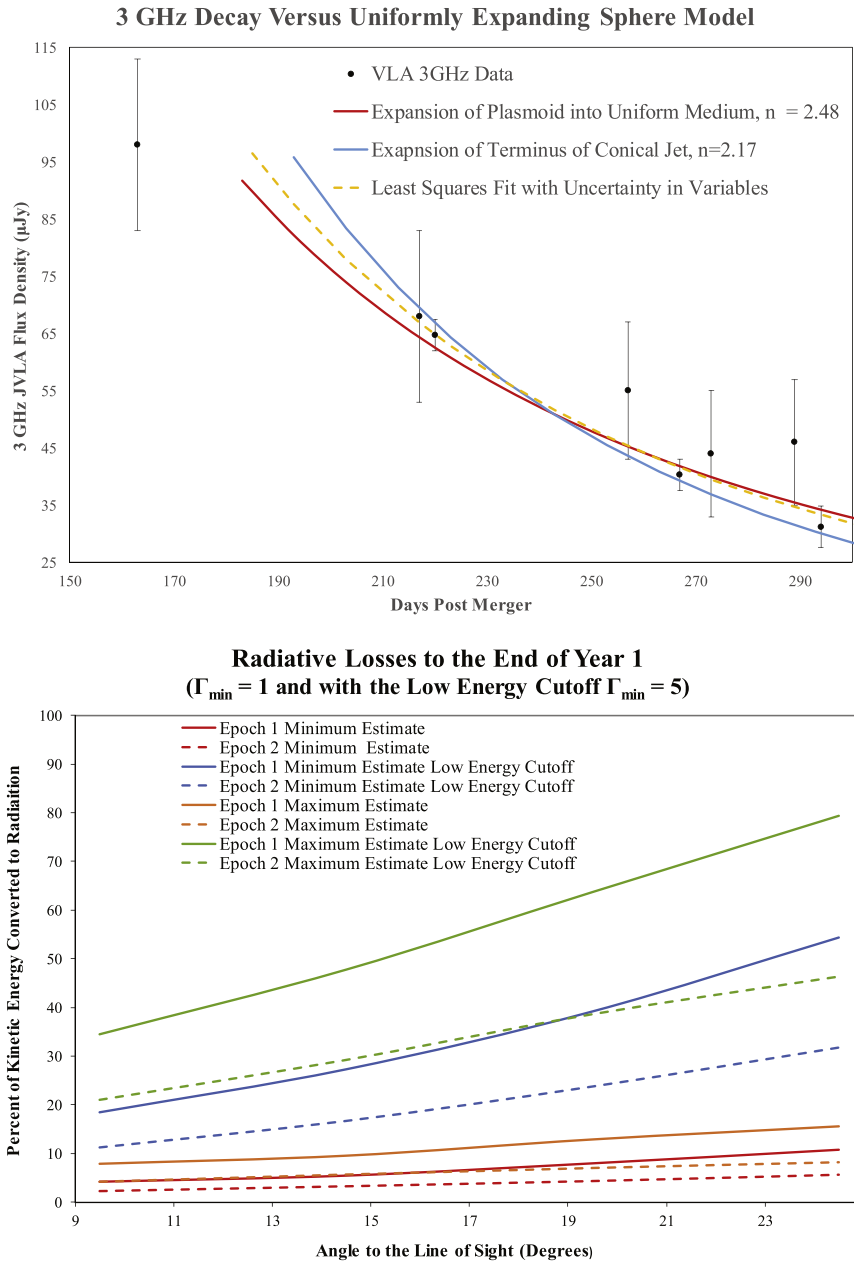


Figure 5. Other constraints on the models. The top panel compares the decay from the peak of the 3 GHz light curve in the models to that of the least squares fit to the data. The bottom panel shows that radiative losses are too large for the discrete ejection model unless $\Gamma_{\min} = 1$. The maximum and minimum conditions are described in the text.

Based on superluminal ejections in the Galaxy, the jet is chosen to be leptonic, but see the Conclusion (Fender et al. 1999; Punsly 2012). The protonic kinetic energy is

$$E(\text{protonic}) = (\gamma - 1)Mc^2, \quad (15)$$

where M is the mass of the plasmoid.

Figures 3 and 4 show the details of the models of Section 2 that are constrained by the fits in Figure 1 and the kinematics in Figure 2. The top-left frame of Figure 3 shows the dependence on $E(lm)$ of both the jet power (the combination of Poynting flux and bulk leptonic internal energy flux) and the baryonic bulk kinetic energy, $E(\text{protonic})$, for one particular LOS. Other LOS produce similar curves. The figure shows the direction (the arrows) of change in jet power and $E(\text{protonic})$ as B and \mathcal{N} vary. The solution with minimum $E(lm)$ has historically been of much

interest in astrophysics. Discrete plasmoids ejected from the GBH, GRS 1915 + 105, evolve toward the minimum energy configuration at late times (Punsly 2012). For a jet model, terminating hot spots in extragalactic jets might be analogous to the high surface brightness feature detected in Mooley et al. (2018a) and it has been argued that hot spots tend to be near minimum energy (Hardcastle et al. 2004). Thus motivated, the bottom panel of Figure 3 shows how the jet power and $E(\text{protonic})$ of the minimum energy solutions (that create the fits in Figure 1) vary with the LOS. Figure 4 shows the physical parameters in the head of the jet or discrete plasmoid for the minimum energy solution, B , R , and the total number of particles (leptons for the jet and baryons for the discrete plasmoid). Note that the fit to the 675 MHz data in epoch 1A has a similar jet power and particle number to epoch 1, but R is 37% larger.

5. Analysis of Results

Due to the low value of the flux densities used to generate these results, both the epoch 1 and epoch 2 data are valuable for constraining the parameters of the outflow. We note from Figures 3 and 4 that R , B , and Poynting flux are very similar in both epochs and these are considered the most robust results. This section is primarily concerned with constraints imposed by X-ray losses and the temporal behavior of the flare decay.

Temporal decay is a standard tool in the analysis of GRBs. This analysis is hindered by the low flux densities. For example, we do not use the Australia Telescope Compact Array 7.25 GHz data during the decay after day 183 because in spite of long ~ 11 hr observations, the flux calibration has a potential 25% systematic error in some or all of the observations (Mooley et al. 2018b; Troja et al. 2018b). We use only the 3 GHz flux densities from the JVLA in the top panel of Figure 5, as they are larger and the JVLA has higher sensitivity (Alexander et al. 2018; Mooley et al. 2018b). The dashed yellow line is the least squares fit with uncertainty in both variables, and the power-law decay constant, $S_\nu(t) \sim t^{-\zeta}$, is $\zeta = 2.30 \pm 0.24$. First we compare this to the discrete uniform, spherical, adiabatic model of van der Laan (1966) that begins expanding into a uniform medium after day 180. The radius of the plasmoid scales like $R(t) \sim t^\omega$, with $S_\nu(t) \sim t^{-2n\omega}$, $\omega = 0.4$ (van der Laan 1966). The analysis raises the uncertainty imposed by small flux densities; Alexander et al. (2018) found $\alpha = 0.74 \pm 0.2$ or $n = 2.48$ on day 217, yet Mooley et al. (2018b) estimated $\alpha = 0.584$ or $n = 2.17$ from their analysis. A value of $\omega = 0.42$ and $n = 2.48$ is implemented in Figure 5 that results in $\zeta = 2.08$ within the standard error of the least squares fit.

Next, we consider the adiabatic expansion of the head of the jet. From Equation (11) and the scalings of the other quantities with spherical expansion in Equation (6) from Moffet (1975), $\zeta = \omega(0.5 - 1.5n)$ for the jet solution. The decay from an expanding head of a conical ($\omega = 1$, Blandford & Königl 1979) Poynting jet is plotted in Figure 5, with $n = 2.17$. $\zeta = 2.76$ in top panel of Figure 5, which exceeds the standard error in the least squares fit. This result is highly dependent on the value of ω . The value of ω assumes that the jet head is collimated by the hoop stresses of the toroidal field, but this might not be the case in an external environment. The conclusion of Figure 5 is that the data quality is insufficient to reject either model or to claim a better fit of one model over the other.

The X-ray radiative losses are prodigious after day 163 (110) with an average apparent luminosity of $3.3 \times 10^{39} \text{ erg s}^{-1}$ ($3.5 \times 10^{39} \text{ erg s}^{-1}$) until the end of year 1 post-merger (Nynka et al. 2018; Troja et al. 2018a, 2018b). The X-ray luminosity varies in consort with the radio luminosity (Troja et al. 2018b). Thus, the same δ might apply to both. By Equation (7) and Figure 2, the intrinsic radiative losses are one or two orders of magnitude less than the apparent luminosity. Thus, by Figure 3, the energy budget is not a concern for the jet solutions. The bottom frame of Figure 5 indicates maximum and minimum radiative losses until the end of year 1 post-merger. The minimum is just the X-ray losses with $\alpha = 0.8$ from 0.3 to 10 keV (Troja et al. 2018b). The maximum is more speculative and assumes a continuous power law from 3 GHz to 10 KeV with $\alpha = 0.584$ (Mooley et al. 2018b). The bottom frame of Figure 5 shows that the losses are too large to be consistent with the $\Gamma_{\min} = 5$ discrete ejection solutions. However, they do not exclude the $\Gamma_{\min} = 1$ solutions if kinetic energy is

transferred to energetic particles through dissipative plasma interactions, possibly with the enveloping medium.

6. Conclusion

Radio imaging data of GW170817 is used to motivate a model of a discrete ejection analogous to active galactic nuclei and compact objects in the Galaxy. It is approximated as a homogeneous spherical volume moving along a preferred axis. Apparent motion in multi-epoch observations constrain the kinematics. B is considered as either turbulent in a baryonic plasmoid or ordered and toroidal in a leptonic Poynting jet. Both solutions are viable based on decay light curves and energetics. The jet power in the models are $2 \times 10^{39} - 8 \times 10^{40} \text{ erg s}^{-1}$. The baryonic ballistic ejection solutions have a kinetic energy of $3 \times 10^{45} - 1.5 \times 10^{47} \text{ erg}$, but require $\Gamma_{\min} \sim 1$ in order to support radiation losses. The main concern with the Poynting jet solutions is that they are very powerful compared to GBH jets. The most energetic ejections from $\sim 10 M_\odot$ GBHs are $\sim 10^{38} \text{ erg s}^{-1}$, if the estimates of Fender et al. (1999), Mirabel & Rodriguez (1994), and Punsly (2012) are recomputed with the new astrometric distance and mass estimates for GRS 1915 + 105 (Reid et al. 2014). The putative post-merger jet efficiency would be orders of magnitude larger than anything ever observed in the Galaxy, even for short periods (\sim hours). If proton kinetic energy had been incorporated into the continuous jet models, then the jet power would have been two orders of magnitude larger, making the jet power from the compact object even more extreme.

Neither a jet nor ballistic ejection is favored by this analysis, but both types of ejections are restricted (energetically) by the models. This form of analysis provides an alternative tool to light curve time evolution. These estimates are valid only after day 110 and do not describe the ejection before this. Yet, these energy estimates can be valuable independent information for constraining the dynamics of the merger process.

I would like to thank Om Sharan Salafia, Kunal Mooley, Lekshmi Resmi, and Raffaella Margutti for help with the radio data. This work was supported by the National Radio Astronomy Observatory, a facility of the National Science Foundation operated under cooperative agreement by Associated Universities, Inc. VLA Projects 17B-425, 18B-204, 18B-302. Partial funding for this work was provided by ICRANet.

ORCID iDs

Brian Punsly  <https://orcid.org/0000-0002-9448-2527>

References

- Abbott, B. P., Abbott, R., Abbott, T. D., et al. 2017a, *PhRvL*, **119**, 161101
- Abbott, B. P., Abbott, R., Abbott, T. D., et al. 2017b, *ApJL*, **848**, L12
- Alexander, K. D., Margutti, R., Blanchard, P. K., et al. 2018, *ApJL*, **863**, L18
- Blandford, R., & Königl, A. 1979, *ApJ*, **232**, 34
- Dobie, D., Kaplan, D., & Murphy, T. 2018, *ApJL*, **858**, 15
- Fender, R., Belloni, T., & Gallo, E. 2004, *MNRAS*, **355**, 1105
- Fender, R., Garrington, S. T., McKay, D. J., et al. 1999, *MNRAS*, **304**, 865
- Ghirlanda, G., Salafia, O. S., Paragi, Z., et al. 2018, arXiv:1808.00469
- Ginzburg, V., & Syrovatskii, S. 1965, *ARA&A*, **3**, 297
- Ginzburg, V., & Syrovatskii, S. 1969, *ARA&A*, **7**, 375
- Goldstein, A., Veres, P., Burns, E., et al. 2017, *ApJL*, **848**, L14
- Hallinan, G., Corsi, A., Mooley, K. P., et al. 2017, *Sci*, **358**, 1579
- Hardcastle, M. J., Harris, D. E., Worrall, D. M., & Birkinshaw, M. 2004, *ApJ*, **612**, 729

- Lightman, A., Press, W., Price, R., & Teukolsky, S. 1975, Problem Book in Relativity and Gravitation (Princeton, NJ: Princeton Univ. Press)
- Lind, K., & Blandford, R. 1985, [ApJ](#), **295**, 358
- Margutti, R., Alexander, K. D., Xie, X., et al. 2018, [ApJL](#), **856**, L18
- Mirabel, I. F., & Rodriguez, L. 1994, [Natur](#), **371**, 46
- Moffet, A. 1975, in Stars and Stellar Systems: Galaxies and the Universe, Vol. 9 ed. A. Sandage, M. Sandage, & J. Kristan (Chicago: Chicago Univ. Press), 211
- Mooley, K. P., Deller, A. T., Gottlieb, O., et al. 2018a, [Natur](#), **561**, 355
- Mooley, K. P., Frail, D. A., Dobie, D., et al. 2018b, arXiv:1810.12927
- Mooley, K. P., Nakar, E., Hotokezaka, K., et al. 2018c, [Natur](#), **554**, 207
- Nynka, M., Ruan, J. J., Haggard, D., & Evans, P. A. 2018, [ApJL](#), **862**, L19
- Punsly, B. 2008, Black Hole Gravitohydrodynamics (2nd ed.; New York: Springer)
- Punsly, B. 2012, [ApJ](#), **746**, 91
- Reed, B. 1989, [AmJPh](#), **57**, 642
- Rees, M. J. 1966, [Natur](#), **211**, 468
- Reid, M., McClintock, J. E., Steiner, J. F., et al. 2014, [ApJ](#), **796**, 2
- Resmi, L., Schulze, S., Ishwara Chandra, C. H., et al. 2018, [ApJ](#), **867**, 57
- Reynolds, C., Punsly, B., Kharb, P., O’Dea, C., & Wrobel, J. 2009, [ApJ](#), **706**, 851
- Rueda, J. A., Ruffini, R., Wang, Y., et al. 2018, [JCAP](#), **10**, 006
- Troja, E., Piro, L., Ryan, G., et al. 2018a, [MNRAS](#), **478**, L18
- Troja, E., van Eerten, E. T. H., Ryan, G., et al. 2018b, arXiv:1808.06617
- Tucker, W. 1975, Radiation Processes in Astrophysics (Cambridge, MA: MIT Press)
- van der Laan, H. 1966, [Natur](#), **211**, 1131